Noninvasive hemodynamic assessment, treatment outcome prediction and follow-up of aortic coarctation from MR imaging

Kristóf Ralovich[a)]
Siemens AG, Imaging and Computer Vision, San-Carlos-Strasse 7, 91058 Erlangen, Germany and Technical University of Munich, Boltzmannstrasse 3, Munich 85748, Germany

Lucian Itu
Siemens S.r.l., Imaging and Computer Vision, B-dul Eroilor nr. 5, 500007 Brasov, Romania and Transilvania University of Brasov, B-dul Eroilor nr. 29, 500036 Brasov, Romania

Dime Vitanovski
Siemens AG, Imaging and Computer Vision, San-Carlos-Strasse 7, 91058 Erlangen, Germany and Pattern Recognition Lab, Friedrich-Alexander University Erlangen-Nuremberg, Martensstrasse 3, 91058 Erlangen, Germany

Puneet Sharma, Razvan Ionasec, and Viorel Mihalef
Siemens Corporation, Imaging and Computer Vision, 755 College Road East, Princeton, New Jersey 08540

Waldemar Krawtschuk
Siemens AG, Imaging and Computer Vision, San-Carlos-Strasse 7, 91058 Erlangen, Germany

Yefeng Zheng
Siemens Corporation, Imaging and Computer Vision, 755 College Road East, Princeton, New Jersey 08540

Allen Everett
The Johns Hopkins Hospital, 600 North Wolfe Street, Baltimore, Maryland 21287

Giacomo Pongiglione and Benedetta Leonardi
Ospedale Pediatrico Bambino Gesù, Piazza Sant'Onofrio 4, 00165 Rome, Italy

Richard Ringel
The Johns Hopkins Hospital, 600 North Wolfe Street, Baltimore, Maryland 21287

Nassir Navab
Technical University of Munich, Boltzmannstrasse 3, Munich 85748, Germany

Tobias Heimann
Siemens AG, Imaging and Computer Vision, San-Carlos-Strasse 7, 91058 Erlangen, Germany

Dorin Comaniciu
Siemens Corporation, Imaging and Computer Vision, 755 College Road East, Princeton, New Jersey 08540

(Received 29 August 2014; revised 30 December 2014; accepted for publication 25 January 2015; published 10 April 2015)

Purpose: Coarctation of the aorta (CoA) is a congenital heart disease characterized by an abnormal narrowing of the proximal descending aorta. Severity of this pathology is quantified by the blood pressure drop ($\triangle P$) across the stenotic coarctation lesion. In order to evaluate the physiological significance of the preoperative coarctation and to assess the postoperative results, the hemodynamic analysis is routinely performed by measuring the $\triangle P$ across the coarctation site via invasive cardiac catheterization. The focus of this work is to present an alternative, noninvasive measurement of blood pressure drop $\triangle P$ through the introduction of a fast, image-based workflow for personalized computational modeling of the CoA hemodynamics.
Methods: The authors propose an end-to-end system comprised of shape and computational models, their personalization setup using MR imaging, and a fast, noninvasive method based on computational fluid dynamics (CFD) to estimate the pre- and postoperative hemodynamics for coarctation patients. A virtual treatment method is investigated to assess the predictive power of our approach.
Results: Automatic thoracic aorta segmentation was applied on a population of 212 3D MR volumes, with mean symmetric point-to-mesh error of 3.00 ± 1.58 mm and average computation time of 8 s. Through quantitative evaluation of 6 CoA patients, good agreement between computed blood pressure drop and catheter measurements is shown: average differences are 2.38 ± 0.82 mm Hg (pre-), 1.10 ± 0.63 mm Hg (postoperative), and 4.99 ± 3.00 mm Hg (virtual stenting), respectively.
Conclusions: The complete workflow is realized in a fast, mostly-automated system that is integrable in the clinical setting. To the best of our knowledge, this is the first time that three different settings (preoperative—severity assessment, poststenting—follow-up, and virtual stenting—treatment outcome prediction) of CoA are investigated on multiple subjects. We believe that

in future—given wider clinical validation—our noninvasive *in-silico* method could replace invasive pressure catheterization for CoA. © *2015 American Association of Physicists in Medicine.* [http://dx.doi.org/10.1118/1.4914856]

Key words: coarctation of aorta, blood pressure drop, MRI, segmentation, computational fluid dynamics (CFD)

1. INTRODUCTION

Coarctation of the aorta (CoA) is a congenital defect characterized by a severe narrowing of the aorta, usually distal to the aortic arch. CoA accounts for 5%–8% of the 8 of 1000 congenital heart disease (that is 4–6 of 10 000) live births[1–3] in the USA and an incidence of 3.6% (3.9 of 10 000) in Germany.[4] CoA is the fifth or sixth most common lesion in congenital heart disease (CHD)[5,6] that still results in lower than average life expectancy for patients.[7,8]

The effect of CoA is a stenosis distal to the aortic arch, resulting in pathophysiological processes that restrict the circulation of oxigenated blood through the narrowing. This necessitates increased cardiac output and may lead to left ventricular (LV) hypertrophy. Generally, CoA results in persistent upper body hypertension and lower body hypotension. Treatment options include various surgical repairs, and after the neonatal period, stent implantation and balloon angioplasty.[9–14]

Preoperative evaluation of CoA severity relies predominately on noninvasive arm/leg blood pressure drops or, if anatomy does not make that comparison feasible, estimation by Doppler ultrasonography. Alternatively, CoA is characterized[8] by greater than 50% narrowing of the aorta as compared to the diaphragmatic aorta diameter. Nevertheless, the clinical gold-standard is obtained by invasive cardiac catheterization to measure $\triangle P$ across the coarctation site. Systolic blood pressure drop between the ascending aorta (AAo) and descending aorta (DAo) above 20 mm Hg characterizes severe CoA and serves as an indicator for treatment.[8]

Recently, Doppler ultrasound[15] and phase contrast (PC) MRI based methods[16–18] have been proposed for a noninvasive estimation of $\triangle P$ by using simplified relationships (e.g., modified Bernoulli equation) between flow and pressure. However, these methods were shown to be inaccurate,[19–22] as the Bernoulli equation uses a limited amount of information (peak velocities), whereas computational fluid dynamics based techniques take into account the patient-specific stenosis shape as well as the velocity profile and are thus able to better predict the turbulent and the viscous pressure drops.

Thus, there is a growing need for comprehensive and truthful hemodynamics analysis of CoA for diagnosis, intervention planning, outcome prediction, and assessment of lesion progression. Our work is directed at these goals. Additionally, as the CoA population includes young patients, less invasive and less expensive (reducing fluoroscopy and catheterization) methods are sought after for $\triangle P$ estimation. For these reasons, the attention of clinical researchers turned to computational fluid dynamics (CFD) methods for more faithful characterization of blood flow in the aorta.

In the interest of easing translation of personalized CoA models into wider clinical practice, we set out to meet certain expectations. On this course, we have broadly extended our previous works[23–25] with stent segmentation, post- and virtual stenting (VS) hemodynamic models. Thus, our contribution provides:

- a fast, end-to-end workflow for noninvasive image-based hemodynamic CoA assessment,
- including robust lumen/stent segmentation,
- that is suitable to make the (i) preoperative diagnosis, (ii) predict treatment outcomes through "virtual stenting" and to (iii) follow-up stented CoA.

2. BACKGROUND

The field of image-based personalized computational hemodynamics was pioneered in 1999 by Taylor *et al.*[26] Since then, the approach was adapted to various organs, from vessels of lower extremities through cardiac hemodynamics[27,28] to cerebral aneurysms.[29,30]

The first step in an image-based simulation is the definition of the computational domain. For CoA investigation, this is the lumen of the thoracic arterial tree. Ongoing imaging research has been directed at segmenting the thoracic aorta from 3D images. Various marching-based approaches were introduced for MRI,[31,32] and machine learning based automatic aorta detection[33] was successfully combined with shape models and applied in intraoperative guidance, based on rotational C-arm CT volumes.

All three of these segmentation approaches consider the aorta only. For our investigation, the supra-aortic arteries are of great importance, as the blood flow that leaves the aortic arch through these vessels (approximately 35%) should be considered in the hemodynamic simulation.[34] On high resolution 3D CT angiograms, the feasibility of accurate carotid artery segmentation was extensively demonstrated.[35] Segmentation of the aorta, including the supra-aortic arteries from MRI, was initially presented in our previous work.[24,25]

Multiple groups investigated CoA hemodynamics through computational modeling. Recent studies have suggested that good agreement may be reached between measured and simulated hemodynamic and morphologic indices if subject-specific boundary conditions are employed.[34,36]

Kim *et al.*[37] developed a personalization scheme with state-of-the-art boundary conditions, coupling the aorta with a lumped parameter description of the left side of the heart. Coogan *et al.*[38] extended the model with elastic vessel wall properties in order to simulate effects of change in

distensibility and stiffness in virtual CoA repair. LaDisa *et al.*[39] employed a similarly sophisticated simulation procedure and concluded that stent implantation does not notably increase the LV workload. Even though these methods ensure high fidelity, imaging data were specifically acquired for the studies, and the long computational times (3–10 days on a 96 core super computer) hinder widespread clinical application.

Recently, a larger study of 13 CoA patients was published.[40] The authors combined MR and x-ray angiograms to define the aorta lumen boundaries. Simulation of preoperative blood pressure drop showed remarkable correlation. Furthermore, treatment outcome prediction was performed by relying on poststenting fluoroscopy measurement for the restored aorta diameter.

Besides the above full 3D CFD simulations, there is an increasing interest in utilizing reduced order circulation models.[41] These approaches are known for their computational efficiency and have been applied successfully to various problems.[42,43]

3. METHODS

The proposed clinical workflow is introduced in this section. Figure 1 provides a graphical overview of the computational steps. The section is organized as follows. The clinical protocol is documented in Sec. 3.A. Estimation of aortic and supra-aortic lumen is explained in Sec. 3.B. Next, Sec. 3.C discusses the extraction of the aortic lumen cross sections from 2D + t PC-MR, and the aortic in- and outflow waveform computations. Finally, the hemodynamics computational model and its image-based personalization is introduced (Sec. 3.E) for three CoA use-cases: preoperative (Sec. 3.E.1), poststenting (Sec. 3.E.2) and "virtual stenting" (Sec. 3.E.3).

3.A. Clinical protocol

The standard CoA protocol at our clinical partners includes the following: acquisition of MR images of the thorax and aortic flow, measurement of the blood pressure with catheterization, heart rate, and cuff measurement at the upper extremities.

MR patient data were acquired using a heterogeneous set of protocols and vendors (Siemens, Philips, GE), employing 1.5 T scanners. The 3D MR volumes are usually oblique stacks of dimension 256×256 to 512×640 with 56–140 slices, in-plane resolution isotropic 0.605–1.562 mm, slice thickness of 0.889–1.8 mm. Among the 3D volumes were contrast enhanced-MR angiogram (CE-MRA) and Balanced Turbo Field Echo (BTFE) acquisition protocols. Patients were at resting conditions during imaging, and the 3D volumes only consisted of a single, static time frame.

The ECG gated Cine PC-MR images are typically oblique axial time-series encoding through-plane velocities in the isotropic resolution of 0.742–2.083 mm, dimension 126×144 to 384×512, VENC found in the range of $140 - 300$ cm/s (it has been ensured that velocity magnitude wrap-around was not present in the PC-MR data). The slices are routinely positioned to provide two different aorta cross-sections, one somewhere around the aortic root, the other in the DAo (if there is a stent implant, in the direction of the blood flow below the stent location) as illustrated in Fig. 2(a). Each time-series corresponds to one heart cycle and has $n = 20 - 40$ frames per cycle. The heart rates of the examined patients range from $H_R = 60 - 114$ bpm.

The pressure catheterization was performed in a pullback procedure. The $\overline{P_{\text{sy}}}$ and $\overline{P_{\text{di}}}$ cuff measurements were taken at the arms.

3.B. Estimation of personalized aortic vessel tree

An accurate geometrical representation of the lumen boundaries of the aorta and supra-aortic arteries is essential for subsequent simulations. The goal of lumen estimation is to automate the vessel morphology measurement process, with manual intervention reduced to a mostly supervisional manner. We have previously developed[24,25] a fast, machine learning based method to automatically extract the aortic lumen from 3D MR volumes. Here, we will explain this segmentation algorithm in more detail and introduce its extension for poststenting cases.

3.B.1. Model of aortic vessel tree

We model the following anatomic parts [Fig. 2(b)]: aortic root (Ro), aortic arch(Ar), walls of AAo and DAo, and the trunk of supra-aortic arteries—brachiocephalic trunk (Br), left common carotid artery (Lc), left subclavian artery (Ls)—and finally, for postoperative cases, the stent region (St). The modeled vessel parts p are abstracted at two levels, (i) pose

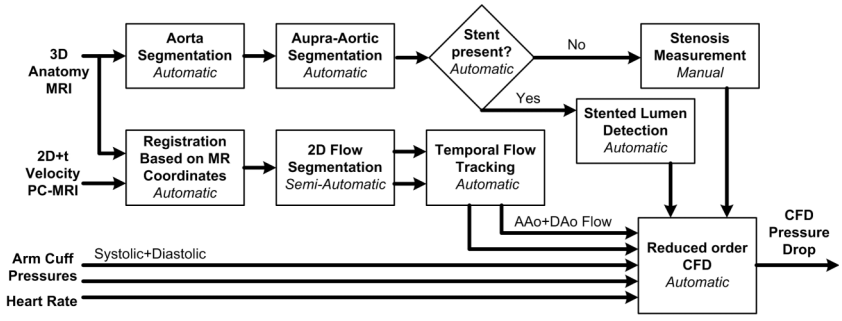

FIG. 1. Overview of our personalized image-based quasi 1D hemodynamic simulation workflow.

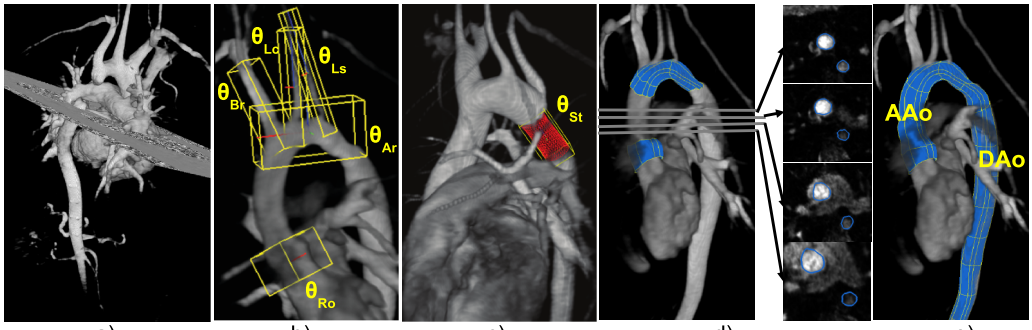

FIG. 2. (a) Standard CoA MR exam with pair of images: 3D MRA and 2D + t PC-MRI. Note the MR signal drop-out at the stented isthmus. (b) θ_o similarity transforms of model parts $o \in \{\text{Ro, Ar, Br, Lc, Ls}\}$. (c) Similarity transform and surface of stent model. (d) Shape models initialized at θ_{Ro} and θ_{Ar}, and circle tracking in axial slices to (e) initialize ascending- and descending aortic walls.

(i.e., similarity transform) and (ii) lumen surface as a dense point distribution.

The pose of the anatomic object part o is denoted by $\theta_o = [\mathbf{t},\mathbf{r},\mathbf{s}]$, where the 9-vector $\mathbf{t}$, $\mathbf{r}$, $\mathbf{s} \in \mathbb{R}^3$ are the position, orientation and size of the object in the 3D image volume I and $o \in \{\text{Ro,Ar,Br,Lc,Ls}\}$. We may write the complete pose parameter estimation as an optimization problem:

$$\begin{aligned}\boldsymbol{\theta}^* &\equiv [\theta^*_{\text{Ro}},\theta^*_{\text{Ar}},\theta^*_{\text{Br}},\theta^*_{\text{Lc}},\theta^*_{\text{Ls}}] \\ &= \underset{\theta_{\text{Ro}},\theta_{\text{Ar}},\theta_{\text{Br}},\theta_{\text{Lc}},\theta_{\text{Ls}}}{\arg\max} P(\theta_{\text{Ro}},\theta_{\text{Ar}},\theta_{\text{Br}},\theta_{\text{Lc}},\theta_{\text{Ls}}|I),\end{aligned} \tag{1}$$

where $\boldsymbol{\theta}^*$ represents the optimal pose parameters of the parts given MR volume I.

3.B.2. Database guided model estimation

Unfortunately, the joint estimation problem in Eq. (1) does not have an analytic solution in general. We address this by decomposing the argument to be estimated sequentially.

By analyzing the database of our annotated volumes, we have observed that the aortic root and arch appear to be the most distinctive objects to be detected. However, their relative pose with respect to each other is strongly scattered due to disparate AAo morphology of patients. With differences in MRI field-of-view, their position in I is also variable. Thus, search for {Ro,Ar} is performed independently in the whole image I. On the other hand, during the review of the annotated vessels, we have noted that the supra-aortic arteries are almost always branching off the same arch region and it makes sense to represent the prior knowledge of this anatomic dependency as spatial constraints in our model. The same principle is true for the stented CoA region that is located at the aortic isthmus with its pose in low variance relative to θ_{Ar}. This allows for a sequential decomposition, thus we may rewrite the argument of Eq. (1):

$$\begin{aligned}&P(\theta_{\text{Ro}},\theta_{\text{Ar}},\theta_{\text{Br}},\theta_{\text{Lc}},\theta_{\text{Ls}},\theta_{\text{St}}|I) \\ &\quad = P(\theta_{\text{Ro}}|I)P(\theta_{\text{Ar}}|I)\prod_{o_i\in\{\text{Br,Lc,Ls,St}\}} P(\theta_{o_i}|\theta_{\text{Ar}},I).\end{aligned} \tag{2}$$

Anatomic dependencies between the parts allow us to reduce the search-space and focus only on the most probable locations/poses during search, formalized in

$$P(\theta_{o_i}|\theta_{\text{Ar}},I) = f(\theta_{o_i}|\theta_{\text{Ar}})P(\theta_{o_i}|I), \tag{3}$$

for parts $o_i \in \{\text{Br,Lc,Ls,St}\}$. In other words, we include a pair-wise prediction weight $f(\theta_{o_i}|\theta_{\text{Ar}})$ describing the likelihood of pose of o_i given the known pose of the aortic arch.

The vessel part estimation is expressed as the inference of the pose parameters from the MR volumes. To estimate the posterior distributions, we propose to use discriminative classifiers. $P(\theta|I) = f(+1|\theta,I)$ is the posterior probability of object presence at θ in a given image I, where f is the learned detector model (fitted using Probabilistic Boosting Tree[44] and 3D Haar features). The pair-wise spatial anatomic constraints [$f(\theta_i|\theta_j)$, the priors] are modeled as Gaussian distributions, which are aggregated over the available training data. We formulate the above pose estimation task in the multiobject detection Integrated Detection Network (IDN)[45] framework.

On unseen images, the learned model is applied in a sliding window manner to detect the anatomic parts. In the hierarchical scheme from Eq. (3), we first estimate the pose of Ro and Ar (performed on the whole MR volume). Subsequently, based on θ_{Ar} and the learned anatomic constraints, the search spaces for the rest of the parts are predicted around the most likely locations. In the proximity of these candidate locations, a localized search follows for {Br,Lc,Ls,St}.

3.B.3. Lumen surface estimation

The second phase of the segmentation procedure estimates the lumen boundaries as tessellated surfaces (dense point distributions). This relies on the bounding boxes (θ_o) of the anatomic "skeleton" computed in the previous step, to initialize shape models and apply learning based boundary detectors[33,45,46] to refine them toward the true lumen boundaries.

The walls of the ascending and descending aorta are treated separately. Their pathological morphology and large length variability do not allow for compact statistical representation. The surfaces of the AAo, DAo are assembled from individual circles, tracked on axial slices of the volume, to connect the root with the arch (for AAo) and descend from the arch to

the diaphragm level (for DAo). Circles are initialized from the previous slice, and contours are refined by in-plane radial boundary detectors, similar to the ones applied in the shape models.[33]

The final lumen model is obtained by merging the separately estimated surfaces. From the lumen surface meshes, four connected centerlines are computed, one for the aorta and three for the supra-aortic arteries.

The explicit modeling of the stented isthmus was necessitated by the fact that poststenting 3D MR volumes have a signal drop-out inside the metallic stent, which "hides" the normal appearance of the aortic lumen, even when contrast agent is present [Fig. 2(a)]. To address this, postoperative volumes are detected by checking the histogram of the volume along the centerline of the segmented aortic isthmus. Near-zero intensity regions signify the loss of the MR signal, in which case the θ_{St} detector is applied. The stent is estimated as a linearly tapering tubular surface connecting the transverse arch and the lower descending aorta.

All MR studies were performed with the patient in supine position, which allowed the oblique volumes to be resampled to a stack of axial slices and reduce variance in the aorta appearance before segmentation. The anisotropic volumes were subsampled on a 3–1 mm Gaussian pyramid of uniform grids. The similarity transform of the vessel parts are detected on 3 mm images, while the lumen boundary detector is run on the finer 1 mm volume.

3.C. Estimation of the patient-specific blood flow from PC-MRI

To quantify each subject's measured aortic blood flow conditions, a velocity encoded $2D+t$ PC-MRI cine image slice is used. These sequences contain through-plane blood flow measurements in an oblique arrangement, intersecting the aorta twice: at the root of ascending aorta and in the region of the descending aorta distal from the CoA. As both MRI images are acquired with the assumption that the patient does not move in the scanner in between, MRI machine coordinates allow for a coarse registration of the MR anatomy and the PC-MR plane. Thus, given the centerline of the aorta calculated from the previous segmentation, delineation of aortic flow boundaries on the PC-MR image plane is initialized using the lumen contour from the 3D surface mesh (Sec. 3.B) and refined by graph cuts.[47] The single time-point segmentation is then tracked throughout the cardiac cycle, propagating the contour based on deformable registration[48] of the n time frames in the cine series. In the patches inside each contour, sampling of the PC-MR image is performed at the pixel centers to obtain velocity values over the entire cardiac cycle. These velocity fields are integrated over the area of the patches to derive the measured ascending- and descending aortic blood flow rates (q_{asc} and q_{desc}).

3.D. Axisymmetric arterial tree construction

Along the centerlines, the lumen surfaces are partitioned into 9 segments (Fig. 3). For each linear tapering tube segment, the length l and proximal r_{in} and distal r_{out} radii are computed: $S_i = \{l, r_{in}, r_{out}\}$, $i \in \{0,\ldots,8\}$ from the 3D lumen surfaces. The 3D mesh is cut with planes perpendicular to the centerlines at the ends of the 9 segments to yield vessel cross-section contours. The radii of the respective segment ends are calculated from the perimeter of these contours. The length of the segments is measured between the cutting planes along the vessel centerlines. Thus the 1D mesh approximates the 3D lumen surface with exact cross-sectional areas at the segment ends, and the lengths of the segments are also preserved. S_7 is either the CoA narrowing or the stent. The start and end cross-sections of the coarctation were taken as the locations where the radius decreases under 95% of the aorta diameter downstream the left-subclavian trunk, and, respectively, increases above 95% of the reference value for the diaphragmatic aorta.

3.E. Axisymmetric quasi 1D CFD FSI

For pressure-drop computations in clinical settings, the total execution time of the algorithm is of paramount

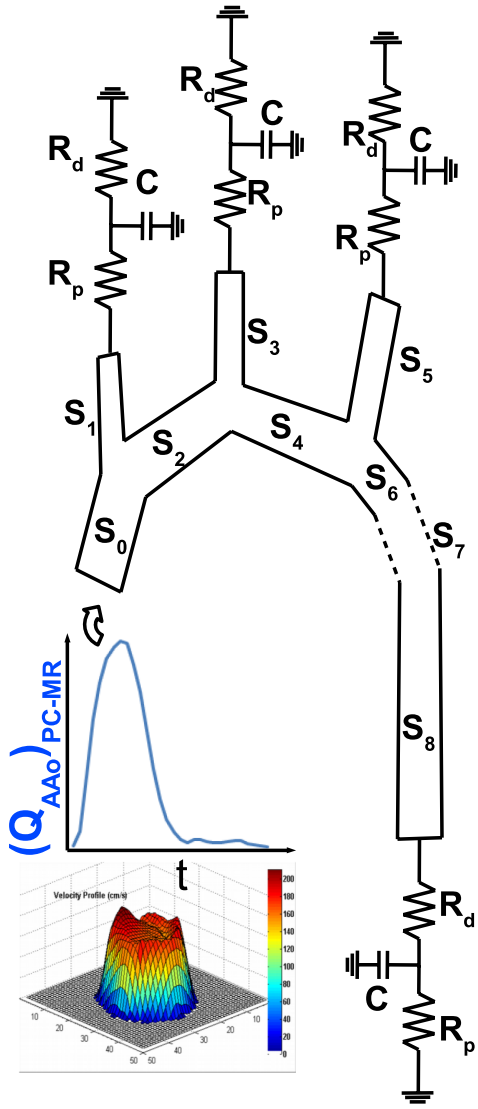

FIG. 3. Arterial tree with discrete axisymmetric segments and terminal boundary conditions.

importance. Thus, we have chosen a reduced-order, quasi 1D circulation model for the aorta. The model consists of the mass [Eq. (4)] and momentum [Eq. (5)] conservation equations, and a state equation for purely elastic[42] wall deformation [Eq. (6)]

$$\frac{\delta A(x,t)}{\delta t}+\frac{\delta q(x,t)}{\delta x}=0, \tag{4}$$

$$\frac{\delta A(x,t)}{\delta t}+\frac{\delta}{\delta x}\left(\alpha\frac{q^2(x,t)}{A(x,t)}\right)+\frac{A(x,t)}{\rho}\frac{\delta p(x,t)}{\delta x}=K_R\frac{q(x,t)}{A(x,t)}, \tag{5}$$

$$p(x,t)=\frac{4}{3}\frac{E\cdot h_i}{r_0}\left(1-\sqrt{\frac{A_0}{A(x,t)}}\right)+p_0, \tag{6}$$

where r_0 is the initial radius corresponding to diastolic pressure p_0. Terminal windkessel elements are applied at the outlets to close the system of equations

$$\frac{\delta p}{\delta t}=R_p\frac{\delta q}{\delta t}-\frac{p}{R_d\cdot C}+\frac{q(R_p+R_d)}{R_d\cdot C}, \tag{7}$$

please refer to the Appendix for a complete listing of notations.

To build the discretized geometric mesh from the centerline and cross-sectional areas, we use an approach similar to previously introduced ones[43], wherein for each vessel of the arterial model, we use several distinct 1D segments S_i with longitudinally varying cross-sectional area values in order to obtain an axisymmetric geometry representation (see Sec. 3.D) of the 3D geometry acquired through MRI. Boundary conditions at the ascending aortic inlet are dictated by the time-varying flow rate q_{asc} computed from PC-MRI (Sec. 3.C).

We use a finite difference solver with patient-specific fixed time step and explicit stability constraints.[23]

In all of our computations, we apply a Newtonian rheological model, where the blood density and dynamic viscosity are set to literature-based values for healthy individuals. The following sections describe the estimation of the wall properties and the windkessel parameters at the outlets.

3.E.1. Preoperative model personalization and configuration

Physiologically motivated three-element windkessel boundary conditions[49,50] require estimation of three parameters (two resistances: proximal - R_p, and distal - R_d, and one compliance - C) at each outlet from measured patient data. The mean arterial pressure ($\overline{P_A}$) is linked to the total vascular resistance by the following relationship: $\overline{P_A}=Q\cdot R$. Here, $\overline{P_A}$ is defined as the average blood pressure over the cardiac cycle, being responsible for perfusion, while Q is the average flow at a point in the arterial circulation, and R is the total distal arterial resistance. Within the aorta, the following formula applies at each supra-aortic branch: $\overline{P_A}=Q_i\cdot(R_t)_i$, where Q_i is the average flow through outlet i and $(R_t)_i$ is the total resistance (the sum of the two windkessel resistances: $R_t=R_p+R_d$). The noninvasive measurements are used to estimate $\overline{P_A}$ in the ascending aorta: $\overline{P_A}=\overline{P_{\text{di}}}+(1/3+H_R\cdot 0.0012)\cdot(\overline{P_{\text{sy}}}-\overline{P_{\text{di}}})$, where H_R is the heart rate and $\overline{P_{\text{sy}}}$ ($\overline{P_{\text{di}}}$) are the systolic (diastolic) cuff-based blood pressures.[51] The combined flow of the supra-aortic outlet vessels is the difference of the MR measured averaged aortic in- and outflow: $Q_{\text{supra-aortic}}=Q_{\text{asc}}-Q_{\text{desc}}$. We use the square law of Zamir *et al.*[52] which establishes a relationship between the radius of major branches of the aorta (supra-aortic branch i) and the flow these branches carry (Q_i):

$$Q_i=Q_{\text{supra-aortic}}\cdot r_i^2/\sum_{j=1}^{3}r_j^2. \tag{8}$$

As there is only a negligible pressure difference between the ascending aorta and the supra-aortic arteries, the same average arterial pressure is used to compute the resistance of each supra-aortic branch

$$(R_t)_i=\overline{P_A}/Q_i. \tag{9}$$

For coarctation patients, the above assumption does not hold for the descending aorta because the narrowing introduces a pressure drop, which is expressed as a flow-dependent resistance $R_c(q)$. Accordingly, the total resistance of the descending aorta is computed from

$$(R_t)_{\text{desc}}+R_c(q)=\overline{P_A}/Q_{\text{desc}}. \tag{10}$$

One of the assumptions made during the derivation of the reduced-order model is that the axial velocity is dominant and the radial components are negligible. This assumption holds well for normal, healthy vessels, but in case of sudden changes in lumen diameter, e.g., for a narrowing like the coarctation, the radial components can no longer be excluded. Thus, for the coarctation segment we use the previously introduced comprehensive pressure drop model:[23]

$$\Delta P=K_v(\omega)R_{\text{vc}}q+\frac{\rho K_t}{2A_{\text{DiAo}}^2}\left(\frac{A_{\text{DiAo}}}{A_c}-1\right)^2|q|q$$
$$+K_uL_u\frac{\delta q}{\delta t}+K_c(\omega)R_{\text{vc}}q, \tag{11}$$

where the four terms represent: the viscous energy losses, the turbulent energy losses due to sudden expansion, the inertial effects and a continuous pressure-flow component. $K_v=1+0.053\cdot\omega^2A_c/A_{\text{DiAo}}$ is the viscosity coefficient and $R_{\text{vc}}=8\ \mu/\pi\int_0^{L_c}1/r^4(l)dl$ is the viscous resistance and $L_u=\rho/\pi\int_0^{L_c}1/r^2(l)dl$ is the inertance; $K_c=0.0018\omega^2$ is the continuous coefficient. Similarly, the morphological CoA stenosis rate (T_{CoA}) is computed from the segmented lumen surfaces as $T_{\text{CoA}}=(1-A_c/A_{\text{DiAo}})$ (see the Appendix for notation). The flow-dependent resistance of the coarctation segment is computed as an average of the individual resistance values of each time frame

$$R_c(q)=\left(\sum_1^n\frac{\triangle P(q_{\text{desc}}(t))}{q_{\text{desc}}(t)}\right)/n, \tag{12}$$

where $\triangle P(\bullet)$ is computed through Eq. (11). Next, a total compliance value of the systemic circulation is determined[49] (C_{tot}). The sum of the outlet compliances (C_{out}) is then computed by subtracting the sum of the compliances of the proximal vessels (C_{prox}) from the total compliance. (C_{out}) is then distributed based on a quadratic power law to the outlets.

Afterward, the mechanical properties of the compliant vessel walls are estimated using a method based on wave

speed estimation.[41] The aortic wall properties are determined from the wave speed c as follows:

$$c = \sqrt{\frac{2}{3\rho}\frac{E \cdot h_i}{r_0}}, \tag{13}$$

where $c = \triangle x / \triangle t$ is computed using the transit-time method[53]: $\triangle x$ represents the distance between the inlet plane at the aortic root and the outlet plane at the descending aorta, and $\triangle t$ is the interval of time during which the flow waveform travels between the two planes. Next, the quantity $E \cdot h_i / r_0$ of all aortic segments, in Eq. (13), is computed as:

$$\frac{E \cdot h_i}{r_0} = \frac{3\rho c^2}{2}. \tag{14}$$

Since the time-varying flow rate (and thus pulse transit information) at the individual supra-aortic branches is not known, a different method is applied for these vessels. The estimation of their wall properties is based on the supposition that arterial bifurcations lead to minimal reflections of forward propagating waves.[54] Hence, first the reflection coefficient at bifurcation k is computed using:[55]

$$\Gamma_k = \frac{Y_p - \sum_i (Y_d)_i}{Y_p + \sum_i (Y_d)_i}, \tag{15}$$

where Y_p and Y_d represent the characteristic admittance (inverse of the characteristic resistance) of the parent and daughter vessels, respectively. Next, the characteristic resistance of the daughter vessel which is a supra-aortic branch is determined by setting Γ equal to 0:

$$R_{\text{supra-aortic}} = \frac{R_{\text{aorta}-p} \cdot R_{\text{aorta}-d}}{R_{\text{aorta}-d} \cdot R_{\text{aorta}-p}}. \tag{16}$$

Finally, the wall properties $(E \cdot h_i / r_0)$ for the supra-aortic branch i are determined as:[23]

$$\frac{E \cdot h_i}{r_0} = \frac{3 \cdot Z_i \cdot \pi^2 \cdot r_0^4}{2 \cdot \rho}. \tag{17}$$

3.E.2. Postoperative model personalization and configuration

In the postoperative configuration, since the same type of information is available as for the preoperative configuration, the model personalization is performed similarly. None of the postoperative models had residual coarctations. As a result: (i) The stented coarctation segments are modeled as regular 1D segments, with large stiffness (the wave speed is approx. 15-times higher than the wave speed of a regular healthy aortic segment). Since the wave speed of the stent is fixed and the length is known, the transit time along the stented segment can be computed directly [the stented segment is excluded from the computation of wave speed in Eq. (13)], (ii) $R_c(q)$ is considered negligible and the total resistance of the windkessel model applied at the outlet of the descending aorta is computed directly from Eq. (10).

3.E.3. Virtual stenting configuration

A third configuration considered in this study consists of performing a virtual stenting procedure on the preoperative aortic model. For prediction of blood pressure drop change after stent implantation, the preoperative geometry is altered, by replacing the stenosed segment (S_7) of the arterial tree with a segment of the same length that is interpolating the cross-section information between the diameters of segments S_6 and S_8. This is meant to model the implantation of a straight stent into the isthmus. The inflow rate is identical to the one used in the preoperative configuration and the model personalization from the postoperative configuration is reused.

4. EXPERIMENTS AND RESULTS

To validate our CoA assessment workflow, we have evaluated our models on *in-vivo* patient data. Clinical data were retrospectively collected from cardiac institutes around the world: (i) the FDA approved multicenter Coarctation of Aorta Stent Trial (COAST)[3] and (ii) Ospedale Pediatrico Bambino Gesù (OPBG). We have conducted two experiments, one to quantify the accuracy of 3D lumen segmentation and a second one to characterize the blood pressure drop estimation.

4.A. Segmentation experiments

In this section, we evaluate the proposed method for aorta segmentation on 212 volumes of 99 patients. In each volume, the lumen surface of the aorta and main branches were delineated by an expert operator and converted to a triangular mesh. This annotation was considered as Ground Truth during model training and testing. The accuracy of cross-validated lumen boundary segmentation is detailed in Table I.

4.B. Experiments on CoA blood pressure drop estimation

For the demonstration of the proposed workflow for noninvasive blood pressure drop assessment, we investigated data-sets from 6 CoA patients. From the above mentioned 99 patients, we extracted 9 subjects, for whom the database contained both preoperative and poststenting state. Three of these subjects developed collateral circulation around the coarctation and were excluded from the experiment, leaving 5 patients from COAST and 1 patient from OPBG (Table II).

TABLE I. Lumen surface segmentation accuracy averaged from four-fold cross validation of 212 3D MR volumes. Displayed as symmetric point-to-mesh (Ref. 56) distance metric in mm.

	Mean ± SD	Median
Aorta	1.80 ± 0.26	1.82
Brachiocephalic	3.40 ± 1.89	2.90
Left common	4.59 ± 3.58	3.16
Left subclavian	4.64 ± 3.33	3.06
Complete model	3.00 ± 1.58	2.43

TABLE II. General information on the population of 6 coarctation patients assessed with our blood pressure drop computation method. Flow rate changes are given over a period of one minute.

Patient	Stenting age	Sex	Stenosis rate (T_{CoA}) (%)	AAo in- (%) flow change after stenting (MRI)	DAo out- (%)
#1	18	F	59.14	−24.96	15.89
#3	27	M	37.05	87.56	13.45
#4	12	F	42.86	7.83	−2.32
#5	15	M	37.48	−32.52	−6.75
#6	22	M	41.47	37.98[a]	17.75
#9	11	F	27.61	14.12	−1.07

[a]*See Sec. 5 for details.*

Using the pipeline introduced in Sec. 3, the patient-specific geometric arterial tree model and corresponding time-resolved flow profiles were estimated from the MR images. To make sure that segmentation errors do not influence the simulation outcomes, the vessel tree geometry was reviewed by a manual operator in all cases before simulation.

Given the patient-specific anatomy, measured flow rates at the AAo and DAo, the flow transit time, systolic and diastolic cuff pressures, and heart rate, we performed a noninvasive parameter estimation of the boundary conditions for each patient. Afterward, the simulation (Sec. 3.E) was performed without any further tuning of the parameters. The blood pressure drop estimate across TAA – DAo is reported between the end of segment S_2 and the start of S_8, whereas the clinically more relevant AAo – DAo is measured between the end of S_0 and the start of segment S_8 of the axisymmetric arterial tree. Differences in pressure drop are determined at the time-instant when the flow rate through the descending aorta is maximal (peak-to-peak).

The results obtained for noninvasive pressure drop (CFD) in preoperative CoA are summarized in Table III, together with the invasive pressures obtained from cardiac catheterization (ICATH).

During treatment of the 6 subjects, the stenoses received repair through balloon angioplasty and stent implantation. After the intervention, patients underwent a follow-up examination similar to the first exam. Analogous to the preoperative case, we have performed the processing pipeline (Sec. 3.E.2) to estimate the poststenting hemodynamic conditions. The comparison of measured and estimated blood pressure drop results is displayed in Table IV.

The last clinical use-case is aimed at "predicting" the blood pressure drop of poststenting conditions prior to the treatment. By applying the introduced methodology (Sec. 3.E.3) to preoperative data, clinicians would be able to virtually evaluate the outcome of the stenting in terms of aortic blood pressure drop (Table V). Figures 4(a) and 4(b) show the blood pressure drop results for all three configurations graphically, while pre- and postoperative evolution of computed aortic flow is shown in Fig. 5.

5. DISCUSSION

5.A. Lumen segmentation

Firstly, we studied the static 3D lumen surface extraction accuracy on a wide set of volumes. Note that our 3D lumen segmentation method is capable of processing a wide range of morphological and pathological aorta variations, not only coarctation patients. The accuracy of the fused aortic vessel tree segmentation was evaluated by using the symmetric point-to-mesh distance[56] metric (Table I) in four-fold cross validation setup of the 212 cases, which shows a good agreement of segmentation results. The aorta segmentation accuracy has much improved compared to our previous results[25] due to

TABLE III. Comparison of the pressure obtained from invasive catheterization (Ref. 57) ($\triangle P^{pre}_{ICATH}$) and our proposed noninvasive method ($\triangle P^{pre}_{CFD}$): peak-to-peak blood pressure drops (mm Hg) between AAo-DAo and transverse aortic arch TAA-DAo.

Patient	AAo-DAo			TAA-DAo		
	$\triangle P^{pre}_{CFD}$	$\triangle P^{pre}_{ICATH}$	$\lvert\triangle P\rvert$	$\triangle P^{pre}_{CFD}$	$\triangle P^{pre}_{ICATH}$	$\lvert\triangle P\rvert$
#1	53.85	55	1.14	53.35	53	0.35
#3	11.32	8	3.32	12.10	8	4.10
#4	27.36	30	2.63	31.94	28	3.94
#5	15.74	14	1.74	13.04	18	4.95
#6	7.26	39	31.73	7.43	43	35.56
#9	11.07	8	3.07	11.06	N/A	N/A
$\overline{\lvert\triangle P^{pre}\rvert}$			2.38 ± 0.82[a]			3.33 ± 1.76[a,b]

[a]Excluding case #6 (*see Sec. 5 for details*).
[b]Excluding case #9, as $\triangle P_{ICATH}$ between TAA-DAo was not measured clinically.

TABLE IV. Peak-to-peak poststenting pressure drop in mm Hg. Comparison of invasive catheterization ($\triangle P^{post}_{ICATH}$) measurement and estimate by our noninvasive method ($\triangle P^{post}_{CFD}$).

	AAo-DAo			TAA-DAo		
Patient	$\triangle P^{post}_{CFD}$	$\triangle P^{post}_{ICATH}$	$\lvert\triangle P\rvert$	$\triangle P^{post}_{CFD}$	$\triangle P^{post}_{ICATH}$	$\lvert\triangle P\rvert$
#1	7.15	8	0.84	5.38	6	0.61
#3	−0.92	−2	1.07	−0.14	−9	8.85
#4	1.23	2	0.76	0.70	−1	1.70
#5	1.26	0	1.26	1.02	0	1.02
#6	3.69	4	0.30	0.92	3	2.07
#9	2.35	0	2.35	1.20	N/A	N/A
$\overline{\lvert\triangle P^{post}\rvert}$			1.10 ± 0.63			2.85 ± 3.04[a]

[a]Excluding case #9, as $\triangle P_{ICATH}$ between TAA-DAo was not measured clinically.

the explicit modeling of the stent induced signal drop-off in postoperative volumes. Due to the morphologic variation of the supra-aortic arteries,their lumen segmentation accuracy is below that of the aorta. It was generally observable that the MR images exhibit some loss of signal toward the borders of the volume (e.g., toward the neck of the patient), which resulted in reduced contrast around the supra-aortic arteries. This is a possible explanation for the difference in accuracy.

5.B. Hemodynamic computations

As can be seen from the results [Table III, Fig. 4(a)], the proposed method performs well for most of the preoperative cases. For patients #1, #3, #4, #5, and #9, our simulation ($\triangle P^{pre}_{CFD}$) reproduces the catheterization blood pressure drop ($\triangle P^{pre}_{ICATH}$) within a narrow margin: mean absolute error of $\overline{\lvert\triangle P^{pre}\rvert} = 2.38 \pm 0.82$ mm Hg. During the review of our results for preoperative case #6, we observed an incorrect PC-MR acquisition plane (intersecting the aortic valve and left ventricular outflow tract instead of the AAo) that results in an erroneous inflow boundary condition initialization (see lower left panel of Fig. 5) and drives the simulation off the course of real aortic inflow. We have included this case in the results for symmetry with the other experiments, and to demonstrate the behavior of the method when fed inconsistent data. Our results are comparable to ICATH, especially in the light of the allowed uncertainty involved in ICATH measurements. According to the IEC standard,[57] invasive blood pressure catheters are required to be accurate within ±3% of the absolute value of blood pressure. Looking at the patient data, we may observe that a variety of both mild ($\triangle P_{ICATH} = 8$) and severe ($\triangle P_{ICATH} = 55$) CoA patients are included and that our method is able to accurately recover the blood pressure drop independent of graveness of this condition [Fig. 4(b)].

The goal of stent implantation is to reduce the difference in blood pressure between the upper and lower body, optimally to completely eliminate the pressure drop. Thus, it is reasonable to expect close-to-zero $\triangle P$ values in the poststenting subjects. However, in some cases residual blood pressure drop persists. Our simulation model for poststenting (Table IV) was able to compute very truthful estimates, marked by $\overline{\lvert\triangle P^{post}\rvert} = 1.10 \pm 0.63$ mm Hg. As shown on the lower right panel of Fig. 5, the PC-MR inflow for poststenting patient #9 does not resemble the characteristic ejection curve of the heart. In this case—similar to pre-op patient #6—the MR inflow plane was acquired too low, it does not measure the ascending blood velocity at the aortic root, but includes the leaflet motion of the valve. Nevertheless, the $\triangle P$ estimates even for #9 are quite accurate because most of the PC-MR inflow was still captured correctly. We believe that our stiff stent-wall postoperative model configuration produces results consistent with the effects of stenting.

To predict the intervention outcome in terms of residual blood pressure drop, we proposed "virtual stenting"

TABLE V. Virtual stenting analysis: comparison of computed pressure drop ($\triangle P^{vs}_{CFD}$) and invasively measured poststenting pressure drop ($\triangle P^{post}_{ICATH}$).

	AAo-DAo			TAA-DAo		
Patient	$\triangle P^{vs}_{CFD}$	$\triangle P^{post}_{ICATH}$	$\lvert\triangle P\rvert$	$\triangle P^{vs}_{CFD}$	$\triangle P^{post}_{ICATH}$	$\lvert\triangle P\rvert$
#1	−1.10	8	9.10	−0.79	6	6.79
#3	−0.93	−2	1.06	−0.54	−9	8.45
#4	7.91	2	3.82	4.51	−1	3.83
#5	−2.84	0	3.12	−2.03	0	2.25
#6	0.06	4	4.25	−0.04	3	3.17
#9	7.98	0	7.85	7.88	N/A	N/A
$\overline{\lvert\triangle P^{vs}\rvert}$			4.99 ± 3.00[a]			5.33 ± 2.42[a,b]

[a]Excluding case #6 (*see Sec. 5 for details*).
[b]Excluding case #9, as $\triangle P_{ICATH}$ between TAA-DAo was not measured clinically.

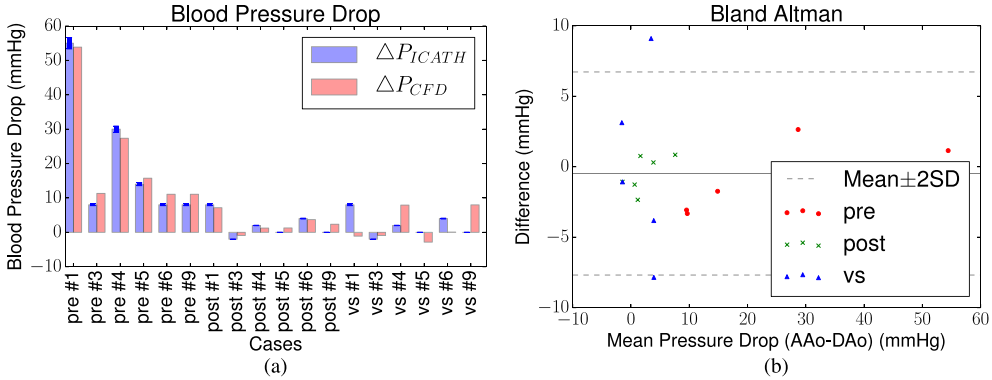

FIG. 4. (a) Absolute values of pre-, post- and virtual stenting blood pressure drop estimates. Allowed uncertainty of $\triangle P_{\mathrm{ICATH}}$ data also shown (Ref. 57) (b) Bland-Altman plot of pressure drop differences[b].

(Sec. 4.B). Here, our model was parameterized to "predict" the pressure drop change attributed to the removal of the obstruction lesion. In Fig. 5, virtual-stenting flow is not shown because a high degree of match between preoperative measured flow and poststenting simulated flow is not our principal aim for this configuration. Instead, this use-case is better characterized by the AAo-DAo pressure drop comparison. The estimated $\triangle P$ is tabulated in Table V and shows a reasonable (4.99 ± 3.00 mm Hg) agreement with the invasively measured poststenting catheter values. It is a well observed process that remodeling of the poststenting aorta is not limited to the vessel wall reinforced by the stent struts: nearby aortic lumen morphology often changes as well, and collateral arteries might reduce or disappear. Without modeling these changes, the mere replacement of the stenosis segment S_7 of the arterial tree will not perfectly forecast the real poststenting vessel and pressure drop, as seen on Fig. 4(b).

Accurate morphological measurement of the stenosis and inflow-rate were shown[58] to have the strongest influence on $\triangle P$ in image-based hemodynamic simulations. As our measured data indicate (Table II), aortic flow rates do change after stenting. This creates an additional challenge for the VS analysis, as only preoperative flow is available for outcome prediction. We believe that this is the second factor behind the largest average error obtained in the VS experiment.

Within these analyses, we have considered all important phases of CoA stenting where currently invasive catheterization is required (severity assessment and posttreatment follow-up) or data are not available (virtual stenting). Our noninvasive results are clinically relevant, especially in comparison with the 20 mm Hg clinical cut-off value, and agree with invasive measurements.

Besides accuracy, the aspect of fast computations is highly desirable in the general clinical practice, and our work

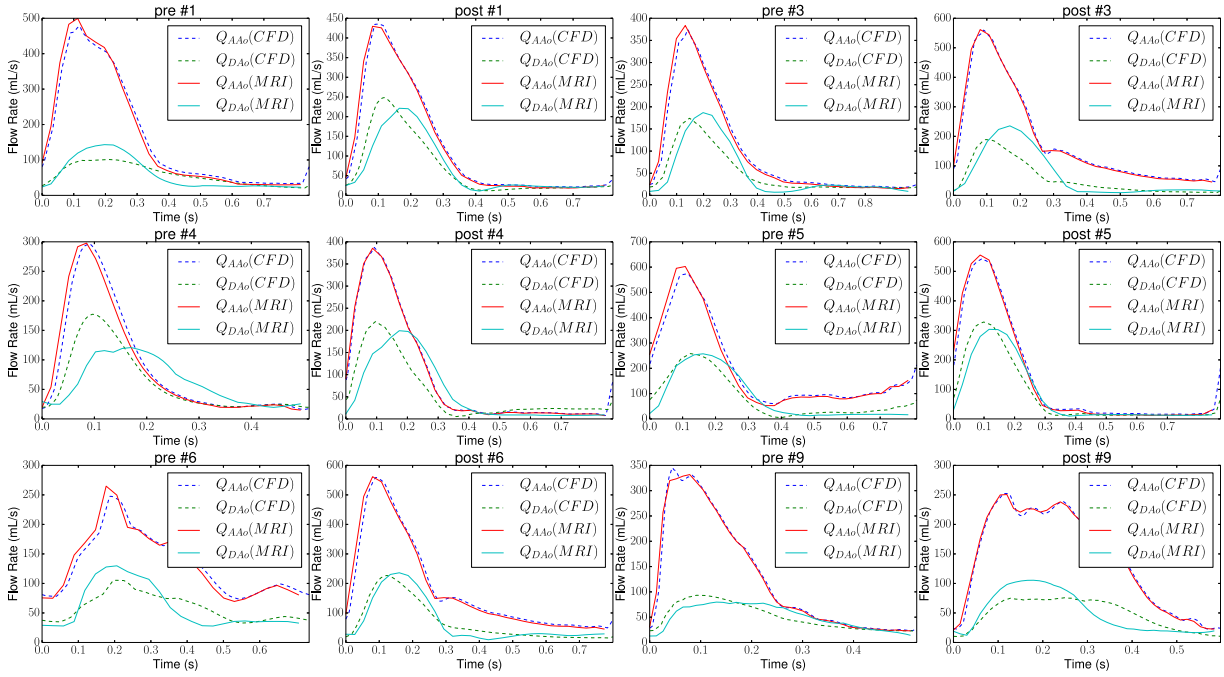

FIG. 5. Temporal evolution of measured (dashed lines) and computed (solid lines) pre- and poststenting flow rates.

TABLE VI. Review of similar hemodynamic CoA assessment research.

	Number of cases			Runtime (h)			Pressure drop, absolute error (mm Hg)		
	Pre-op	Post-op (normal)	Virtual stenting	Segmentation	Meshing	cfd	Pre-op	Post-op/normal	Virtual stenting
LaDisa *et al.* (Ref. 39)	2	3[a]	—	—	—	days[b]	−1.5 ± 4.94	1.66 ± 1.15	—
Valverde *et al.* (Ref. 36)	5	2[a]	—	—	—	—	−4.2 ± 4.9	1.0 ± 1.0	—
Ralovich *et al.* (Ref. 24)	4	—	—	0.5	0.5	8–10	4.57 ± 5.53	—	—
Itu *et al.* (Ref. 23)	4	—	—	—	—	0.13–0.16	1.45 ± 0.76	—	—
Goubergrits *et al.* (Ref. 40)	13	—	13	1–4	—	8	−0.5 ± 0.33	—	3.0 ± 2.91
Current work	6[c]	6	6[c]	0.5	0.25	0.13–0.16	2.38 ± 0.82[c]	1.10 ± 0.63	4.99 ± 3.00[c]

[a]Normal cases were considered in the same group as postoperative (as we expect near-zero $\triangle P$).
[b]Approximated from similar complexity reports (Refs. 37 and 38).
[c]Excluding case #6 (*see Sec. 5 for details*).

provides a first effort to reduce the runtime of CoA simulation workflows. Average detection time of the combined lumen model (for all surfaces) is in the range of 8 s. The semiautomatic PC-MR flow segmentation and contour tracking take approximately one minute per case. Our reduced order CFD model is much faster (8–10 min) than conventional unsteady 3D flow computations (all times measured on an Intel Core i7 laptop computer).

Finally, Table VI shows a quantitative review of state-of-the-art investigations of CoA hemodynamics and illustrates the position of our contributions against literature. The table provides an overview of the questions recent research has addressed, such as the type of clinical use-cases, number of subjects examined, included methods and their run-times. We should note that the subjects are different, and therefore a direct comparison of pressure drop results is not feasible across the different works. Closest to our work is the recent study[40] of 13 patients. The authors performed image-based rigid wall 3D simulations of CoA patients. Their investigation included two CoA use-cases, one for pretreatment estimation of blood pressure drop (very similar to our first experiment), and a second experiment that falls in between our poststenting and virtual stenting use-cases. In the latter, the authors have reconstructed the postoperative aorta geometry from x-ray images after the treatment and used the preoperative PC-MR inflow. As this configuration uses preoperative inflow and postintervention geometry, we compare it against our third experiment. Even though their average error of pressure estimation is lower than ours, several aspects limit the benefits of their workflow: first, the simulation time is an order of magnitude larger than ours, second, the blood flow is simulated only at a single time point (systolic state), and third, their high quality vessel measurements require ionizing fluoroscopy.

In general, most hemodynamic simulation studies investigate cases where the whole patient data acquisition is driven by specific computational needs. On the other hand, our methods work on real clinical images that were acquired retrospectively and not specifically for this computation study. As shown, this comes with its own challenges, for example, the sensitivity of positioning the PC-MR plane or suboptimal image quality. However, a solid advantage is that further validation of our methods would be possible using existing (previously acquired) data.

5.C. Limitations and future works

We have shown that the presented models can be used to assess the blood pressure conditions of CoA. Yet, our method opens several technical and clinical questions.

Our predefined anatomic part and shape model based segmentation method applies only to cases that exhibit shape variation, but do not change in topology. CoA often coincides with other aortic arch morbidities, thus segmentation of pathological vessel configurations (e.g., other than three supra-aortic arteries, loop of aorta, collateral circulation) would be beneficial to be included in the system. Currently, we do not handle such cases automatically.

Secondly, a single plane of velocity encoded cine PC-MR image might not be able to capture the flow of intercostal arteries and collateral vessels. If such arteries are present and bypass the coarctation site, multiple PC-MR planes might be required to capture their flow and the clinical imaging protocol would have to be extended.

Moreover, it would be interesting to quantify the sensitivity of the hemodynamic simulation results as a function of the accuracy of the segmented aorta and coarctation lumen surfaces, similar to Ref. 58.

Future work should be aimed at addressing these points.

6. CONCLUSION

To summarize, our main contribution to the field is an end-to-end pipeline for image-based hemodynamic assessment of blood pressure drop in coarctation of the aorta. The system

was shown to compare well against invasive blood pressure catheterization. The complete workflow is realized in a fast, automated system that can be integrated into a clinical setting, where manual interaction is required in a mostly supervisional manner.

A set of validation experiments (212 cases for aorta segmentation and 6 cases for blood pressure drop) has shown that the proposed methods work on a wide variety of low-quality, retrospective data. The data stems from regular clinical practice of multiple cardiac centers in the USA and the EU and was not explicitly acquired for simulation studies. Furthermore, all data used for parameter personalization were acquired noninvasively, which is important considering the often young age of CoA patients. We have demonstrated that the framework is applicable to three stages of CoA care: preoperative severity assessment, poststenting follow-up, and treatment outcome prediction through "virtual stenting."

We believe that the presented noninvasive *in-silico* method has the potential—given more thorough clinical validation—to replace invasive pressure catheterization for CoA.

ACKNOWLEDGMENTS

This work has been partially funded by European Union Specific Targeted Research Project No. FP7 – 248421 Sim-e-Child (http://www.sim-e-child.org) and, by the Sectoral Operational Programme Human Resources Development (SOP HRD), ID134378 financed from the European Social Fund and by the Romanian Government. The first author was recipient of Ernst von Siemens Promotionsstipendium. The authors would like to acknowledge Dr. Michael Sühling for fruitful discussions, and the reviewers for their constructive comments on this manuscript.

APPENDIX: NOTATION

θ_o	Similarity transform of part o
S_i	Segment i in axisymmetric model of arterial tree
A_{DiAo}	Cross sectional area at diaphragm level (cm^2)
A_c	Coarctation minimum cross sectional area (cm^2)
L_c	Coarctation (preoperative S_7) length (cm)
p	Arterial pressure [$\mathrm{g/(cm\ s^2)}$]
q (Q)	Flow rate, time-varying (constant, averaged) (ml/s)
t	Time (s)
x	Location along centerline (cm)
α	The momentum-flux correction coefficient
ω	Womersley number
ρ	= 1.055, blood density ($\mathrm{g/cm}^3$)
μ	= 4.5, dynamic viscosity (mPa s)
K_R	Friction parameter (cm) [Eq. (5)]
K_t	= 1.52, turbulence coefficient [Eq. (11)]
K_u	= 1.2, inertance coefficient [Eq. (11)]
E	Young's modulus [$\mathrm{g/(cm\ s^2)}$]
h_i	Wall thickness of segment i (cm)
Γ_k	Reflection coefficient at bifurcation k [Eq. (15)]
R	Resistance [$\mathrm{g/(cm^4\ s)}$]
Y	Characteristic admittance [$\mathrm{(cm^4\ s)/g}$]
Z_i	Impedance of supra-aortic i [$\mathrm{g/(cm^4\ s)}$] [Eq. (17)]
T_{CoA}	Stenosis rate (morphologic)
H_R	Heart rate (bpm)
$\overline{P_A}$	Mean arterial pressure [$\mathrm{g/(cm\ s^2)}$]
$\overline{P_{sy}}\left(\overline{P_{di}}\right)$	Systolic (dias.) cuff pressures [$\mathrm{g/(cm\ s^2)}$]
n	Number of PC-MR frames (per cardiac cycle)
c	Pressure wave speed (cm/s) [Eq. (13)]

[a]Electronic mail: ralovich@in.tum.de

[1]J. I. E. Hoffman and S. Kaplan, "The incidence of congenital heart disease," J. Am. Coll. Cardiol. **39**(12), 1890–1900 (2002).
[2]R. E. Ringel, *Covered Cheatham Platinum CP Stents for the Prevention or Treatment of Aortic Wall Injury Associated With Coarctation of the Aorta COAST II* (Food and Drug Administration, Johns Hopkins University, 2010), accessed 22 February 2012, http://clinicaltrials.gov/ct2/show/NCT01278303.
[3]R. E. Ringel and K. Jenkins, *Coarctation Of the Aorta Stent Trial (COAST)* (Food and Drug Administration, Johns Hopkins University, 2007), accessed 10 March 2011, http://clinicaltrials.gov/ct2/show/NCT00552812.
[4]A. Lindinger, G. Schwedler, and H.-W. Hense, "Prevalence of congenital heart defects in newborns in germany: Results of the first registration year of the pan study (july 2006 to june 2007)," Klin. Pädiatrie **222**(05), 321–326 (2010).
[5]H. Dolk, M. Loane, and E. Garne, European Surveillance of Congenital Anomalies (EUROCAT) Working Group "Congenital heart defects in europe: Prevalence and perinatal mortality, 2000 to 2005," Circulation **123**(8), 841–849 (2011).
[6]D. Tanous, L. N. Benson, and E. M. Horlick, "Coarctation of the aorta: Evaluation and management," Curr. Opin. Cardiol. **24**, 509–515 (2009).
[7]M. E. Fawzy, M. Awad, W. Hassan, Y. Al Kadhi, M. Shoukri, and F. Fadley, "Long-term outcome (up to 15 years) of balloon angioplasty of discrete native coarctation of the aorta in adolescents and adults," J. Am. Coll. Cardiol. **43**(6), 1062–1067 (2004).
[8]J. W. Vriend and B. J. Mulder, "Late complications in patients after repair of aortic coarctation: Implications for management," Int. J. Cardiol. **101**, 399–406 (2005).
[9]H. Bentall and A. De Bono, "A technique for complete replacement of the ascending aorta," Thorax **23**(4), 338–339 (1968).
[10]J. S. de Lezo, M. Pan, M. Romero, A. Medina, J. Segura, M. Lafuente, D. Pavlovic, E. Hernendez, F. Melian, and J. Espada, "Immediate and follow-up findings after stent treatment for severe coarctation of aorta," Am. J. Cardiol. **83**(3), 400–406 (1999).
[11]P. Ewert, H. Abdul-Khaliq, B. Peters, N. Nagdyman, S. Schubert, and P. E. Lange, "Transcatheter therapy of long extreme subatretic aortic coarctations with covered stents," Catheterization Cardiovasc. Interventions **63**(2), 236–239 (2004).
[12]D. A. Harrison, P. R. McLaughlin, C. Lazzam, M. Connelly, and L. N. Benson, "Endovascular stents in the management of coarctation of the aorta in the adolescent and adult: One year follow up," Heart **85**(5), 561–566 (2001).
[13]M. Hernández-González, S. Solorio, I. Conde-Carmona, A. Rangel-Abundis, M. Ledesma, J. Munayer, F. David, J. Ortegón, S. Jimanez, A. Sánchez-Soberanis, C. Meléndez, S. Claire, J. Gomez, R. Teniente-Valente, and C. Alva, "Intraluminal aortoplasty vs. surgical aortic resection in congenital aortic coarctation: A clinical random study in pediatric patients," Arch. Med. Res. **34**(4), 305–310 (2003).
[14]B. D. Thanopoulos, L. Hadjinikolaou, G. N. Konstadopoulou, G. S. Tsaousis, F. Triposkiadis, and P. Spirou, "Stent treatment for coarctation of the aorta: Intermediate term follow up and technical considerations," Heart **84**(1), 65–70 (2000).
[15]V. Lee, C. Spritzer, B. Carroll, L. Pool, M. Bernstein, S. Heinle, and J. MacFall, "Flow quantification using fast cine phase-contrast mr imaging, conventional cine phase-contrast mr imaging, and doppler sonography: In vitro and in vivo validation," Am. J. Roentgenol. **169**(4), 1125–1131 (1997).

[16]J. Lotz, C. Meier, A. Leppert, and M. Galanski, "Cardiovascular flow measurement with phase-contrast mr imaging: Basic facts and implementation," Radiographics **22**(3), 651–671 (2002).
[17]M. Markl, P. Kilner, and T. Ebbers, "Comprehensive 4d velocity mapping of the heart and great vessels by cardiovascular magnetic resonance," J. Cardiovasc. Magn. Reson. **13**(1), 7–28 (2011).
[18]N. J. Pelc, R. J. Herfkens, A. Shimakawa, and D. R. Enzmann, "Phase contrast cine magnetic resonance imaging," Magn. Reson. Q. **7**(4), 229–254 (1991).
[19]J. J. Heys, N. Holyoak, A. M. Calleja, M. Belohlavek, and H. P. Chaliki, "Revisiting the simplified bernoulli equation," Open Biomed. Eng. J. **4**, 123–128 (2010).
[20]P. R. Hoskins, "Accuracy of maximum velocity estimates made using doppler ultrasound systems," Br. J. Radiol. **69**(818), 172–177 (1996).
[21]J. Peters, A. Lungu, F. M. Weber, I. Waechter-Stehle, D. R. Hose, and J. Weese, "Comparison of cfd-based and bernoulli-based pressure drop estimates across the aortic valve enabled by shape-constrained deformable segmentation of cardiac ct images," in *Biomedical Simulation* (Springer, Cham, Switzerland, 2014), pp. 211–219.
[22]B. L. Seifert, K. DesRochers, M. Ta, G. Giraud, M. Zarandi, M. Gharib, and D. J. Sahn, "Accuracy of doppler methods for estimating peak-to-peak and peak instantaneous gradients across coarctation of the aorta: An in vitro study," J. Am. Soc. Echocardiography **12**(9), 744–753 (1999).
[23]L. Itu, P. Sharma, K. Ralovich, V. Mihalef, R. Ionasec, A. Everett, R. Ringel, A. Kamen, and D. Comaniciu, "Non-invasive hemodynamic assessment of aortic coarctation: Validation with in vivo measurements," Ann. Biomed. Eng. **41**(4), 669–681 (2013).
[24]K. Ralovich, L. Itu, V. Mihalef, P. Sharma, R. Ionasec, D. Vitanovski, W. Krawtschuk, A. Everett, R. Ringel, N. Navab, and D. Comaniciu, "Hemodynamic assessment of pre- and postoperative aortic coarctation from mr images," in *Medical Image Computing and Computer-Assisted Intervention - MICCAI* (Springer, Berlin Heidelberg, 2012).
[25]D. Vitanovski, K. Ralovich, R. Ionasec, Y. Zheng, M. Suehling, W. Krawtschuk, J. Hornegger, and D. Comaniciu, "Personalized learning-based segmentation of thoracic aorta and main branches for diagnosis and treatment planning," in *9th IEEE International Symposium on Biomedical Imaging (ISBI)* (IEEE, New York, NY, 2012), pp. 836–839.
[26]C. A. Taylor, M. T. Draney, J. P. Ku, D. Parker, B. N. Steele, K. Wang, and C. K. Zarins, "Predictive medicine: Computational techniques in therapeutic decision-making," Comput. Aided Surg. **4**(5), 231–247 (1999).
[27]V. Mihalef *et al.*, "Patient-specific modelling of whole heart anatomy, dynamics and haemodynamics from four-dimensional cardiac ct images," Interface Focus **1**, 286–296 (2011).
[28]K. S. Sundareswaran, D. de Zelicourt, S. Sharma, K. R. Kanter, T. L. Spray, J. Rossignac, F. Sotiropoulos, M. A. Fogel, and A. P. Yoganathan, "Correction of pulmonary arteriovenous malformation using image-based surgical planning," J. Am. Coll. Cardiol.: Cardiovasc. Imaging **2**(8), 1024–1030 (2009).
[29]H.-H. Chang, G. R. Duckwiler, D. J. Valentino, and W. C. Chu, "Computer-assisted extraction of intracranial aneurysms on 3D rotational angiograms for computational fluid dynamics modeling," Med. Phys. **36**(12), 5612–5621 (2009).
[30]Q. Sun, A. Groth, and T. Aach, "Comprehensive validation of computational fluid dynamics simulations of in-vivo blood flow in patient-specific cerebral aneurysms," Med. Phys. **39**(2), 742–754 (2012).
[31]E. Flehmann *et al.*, "Towards patient specific catheter selection: Computation of aortic geometry based on fused mri data," in *Proceedings of the 6th International Conference on Functional Imaging and Modeling of the Heart* (Springer, Berlin Heidelberg, 2011), pp. 145–152.
[32]F. Zhao *et al.*, "Automated 4d segmentation of aortic magnetic resonance images," in *The 17th British Machine Vision Association* (BMVA Press, Durham, UK, 2006), Vol. 1, pp. 247–257.
[33]Y. Zheng, M. John, R. Liao, J. Boese, U. Kirschstein, B. Georgescu, S. K. Zhou, J. Kempfert, T. Walther, G. Brockmann, and D. Comaniciu, "Automatic aorta segmentation and valve landmark detection in c-arm ct: Application to aortic valve implantation," in *Proceedings of the 13th International Conference on Medical Image Computing and Computer-assisted Intervention: Part I* (Springer-Verlag, Berlin, Heidelberg, 2010), pp. 476–483.
[34]D. Gallo, G. Santis, F. Negri, D. Tresoldi, R. Ponzini, D. Massai, M. Deriu, P. Segers, B. Verhegghe, G. Rizzo, and U. Morbiducci, "On the use of in vivo measured flow rates as boundary conditions for image-based hemodynamic models of the human aorta: Implications for indicators of abnormal flow," Ann. Biomed. Eng. **40**(3), 729–741 (2012).
[35]K. Hameeteman *et al.*, "Evaluation framework for carotid bifurcation lumen segmentation and stenosis grading," Med. Image Anal. **15**, 477–488 (2011).
[36]I. Valverde, C. Staicu, H. Grotenhuis, A. Marzo, K. Rhode, Y. Shi, A. Brown, A. Tzifa, T. Hussain, G. Greil, P. Lawford, R. Razavi, R. Hose, and P. Beerbaum, "Predicting hemodynamics in native and residual coarctation: Preliminary results of a rigid-wall computational-fluid-dynamics model (rw-cfd) validated against clinically invasive pressure measures at rest and during pharmacological stress," J. Cardiovasc. Magn. Reson. **13**, 1–4 (2011).
[37]H. Kim, I. Vignon-Clementel, C. Figueroa, J. LaDisa, K. Jansen, J. Feinstein, and C. Taylor, "On coupling a lumped parameter heart model and a three-dimensional finite element aorta model," Ann. Biomed. Eng. **37**, 2153–2169 (2009).
[38]J. S. Coogan, F. P. Chan, C. A. Taylor, and J. A. Feinstein, "Computational fluid dynamic simulations of aortic coarctation comparing the effects of surgical- and stent-based treatments on aortic compliance and ventricular workload," Catheterization Cardiovasc. Interventions **77**(5), 680–691 (2011).
[39]J. F. J. LaDisa, C. Alberto Figueroa, I. E. Vignon-Clementel, H. J. Kim, N. Xiao, L. M. Ellwein, F. P. Chan, J. A. Feinstein, and C. A. Taylor, "Computational simulations for aortic coarctation: Representative results from a sampling of patients," J. Biomech. Eng. **133**, 091008 (2011).
[40]L. Goubergrits, E. Riesenkampff, P. Yevtushenko, J. Schaller, U. Kertzscher, A. Hennemuth, F. Berger, S. Schubert, and T. Kuehne, "Mri-based computational fluid dynamics for diagnosis and treatment prediction: Clinical validation study in patients with coarctation of aorta," J. Magn. Reson. Imaging **41**(4), 909–916 (2014).
[41]M. S. Olufsen, C. S. Peskin, W. Y. Kim, E. M. Pedersen, A. Nadim, and J. Larsen, "Numerical simulation and experimental validation of blood flow in arteries with structured-tree outflow conditions," Ann. Biomed. Eng. **28**(11), 1281–1299 (2000).
[42]P. Reymond, Y. Bohraus, F. Perren, F. Lazeyras, and N. Stergiopulos, "Validation of a patient-specific one-dimensional model of the systemic arterial tree," Am. J. Physiol. Heart Circ. Physiol. **301**(3), H1173–H1182 (2011).
[43]B. N. Steele, J. Wan, J. P. Ku, T. J. Hughes, and C. A. Taylor, "In vivo validation of a one-dimensional finite-element method for predicting blood flow in cardiovascular bypass grafts," IEEE Trans. Biomed. Eng. **50**(6), 649–656 (2003).
[44]Z. Tu, "Probabilistic boosting-tree: Learning discriminative models for classification, recognition, and clustering," in *Proceedings of ICCV* (IEEE Computer Society, Washington, DC, 2005), Vol. 2, pp. 1589–1596.
[45]M. Sofka, K. Ralovich, N. Birkbeck, J. Zhang, and S. Zhou, "Integrated detection network (idn) for pose and boundary estimation in medical images," in *Proceedings of the 8th International Symposium on Biomedical Imaging (ISBI), Chicago, IL, 30 Mar–2 Apr 2011* (IEEE Computer Society, Washington, DC, 2011).
[46]Z. Yefeng, A. Barbu, B. Georgescu, M. Scheuering, and D. Comaniciu, "Four-chamber heart modeling and automatic segmentation for 3-d cardiac ct volumes using marginal space learning and steerable features," IEEE Trans. Med. Imaging **27**(11), 1668–1681 (2008).
[47]Y. Boykov and V. Kolmogorov, "An experimental comparison of min-cut/max- flow algorithms for energy minimization in vision," IEEE Trans. Pattern Anal. Mach. Intell. **26**(9), 1124–1137 (2004).
[48]M.-P. Jolly, C. Guetter, and J. Guehring, "Cardiac segmentation in mr cine data using inverse consistent deformable registration," in *IEEE International Symposium on Biomedical Imaging (ISBI)* (IEEE, Washington, DC, 2010), pp. 484–487.
[49]N. Stergiopulos, D. Young, and T. Rogge, "Computer simulation of arterial flow with applications to arterial and aortic stenoses," J. Biomech. **25**(12), 1477–1488 (1992).
[50]I. Vignon-Clementel, C. Figueroa, K. Jansen, and C. Taylor, "Outflow boundary conditions for 3d simulations of non-periodic blood flow and pressure fields in deformable arteries," Comput. Methods Biomech. Biomed. Eng. **13**(5), 625–640 (2010).
[51]M. Razminia, A. Trivedi, J. Molnar, M. Elbzour, M. Guerrero, Y. Salem, A. Ahmed, S. Khosla, and D. L. Lubell, "Validation of a new formula for mean arterial pressure calculation: The new formula is superior to the standard formula," Catheterization Cardiovasc. Interv. **63**(4), 419–425 (2004).
[52]M. Zamir, P. Sinclair, and T. H. Wonnacott, "Relation between diameter and flow in major branches of the arch of the aorta," J. Biomech. **25**(11), 1303–1310 (1992).

[53]E.-S. H. Ibrahim, K. R. Johnson, A. B. Miller, J. M. Shaffer, and R. D. White, "Measuring aortic pulse wave velocity using high-field cardiovascular magnetic resonance: comparison of techniques," J. Cardiovasc.Magn.Reson. **12**, 26–38 (2010).

[54]G. S. Kassab and Y.-C. B. Fung, "The pattern of coronary arteriolar bifurcations and the uniform shear hypothesis," Ann. Biomed. Eng. **23**(1), 13–20 (1995).

[55]J. Mynard and P. Nithiarasu, "A 1d arterial blood flow model incorporating ventricular pressure, aortic valve and regional coronary flow using the locally conservative galerkin (lcg) method," Commun. Numer. Methods Eng. **24**(5), 367–417 (2008).

[56]Y. Zheng, *Marginal Space Learning for Medical Image Analysis: Efficient Detection and Segmentation of Anatomical Structures* (SpringerLink: Bücher. Springer, New York, NY, 2014).

[57]IEC, "Medical electrical equipment - part 2-34: Particular requirements for the basic safety and essential performance of invasive blood pressure monitoring equipment," in *IEC 60601-2-34* (IEC/ANSI, Geneva, Switzerland, 2011), accessed June 10 2014.

[58]W. Chen, L. Itu, P. Sharma, and A. Kamen, "Uncertainty quantification in medical image-based hemodynamic computations," in *IEEE 11th International Symposium on Biomedical Imaging (ISBI)* (IEEE, Washington, DC, 2014), pp. 433–436.